Effect of Laves Phase on Ductile-Brittle Transition of 12 Pct Cr Steel

J. BORISOVA, V. DUDKO, R. MISHNEV, and R. KAIBYSHEV

The impact toughness of a martensitic 12 Cr-0.6 Mo-2.2 W-4 Co-0.8 Cu-VNb (in wt pct) steel subjected to tempering at 770 °C for 3 hours and aging at 650 °C for 643 hours was examined in the temperature range of − 20 to 250 °C. The steel in the tempered condition exhibits a ductile-brittle transition temperature (DBTT) of 41 °C and a Charpy V-notch impact energy of 100 J/cm^2 at a temperature of 20 °C. The tempered steel becomes completely brittle at 0 °C when the absorbed energy falls to 8 J/cm^2. The aging leads to the precipitation of a Laves phase at boundaries of the tempered martensite lath structure (TMLS). This deteriorates the impact toughness, the DBTT increases to 20 J/cm^2, the impact toughness at a temperature of 20 °C decreases to 20 J/cm^2. Under impact loads, the Laves phase particles serve as additional nucleation sites for micro-crack/void that facilitates unstable crack propagation. As a result, the appearance of cracks with critical dimensions takes place after stable crack propagation over a very short distance, and embrittlement takes place at relatively high temperatures.

https://doi.org/10.1007/s11661-019-05269-y

I. INTRODUCTION

A new generation of 9 to 12 pctCr steels is widely used for turbine components such as steam pipelines, rotors, blades, disks, and valves of fossil power plants, which operate under ultra-super critical conditions with steam pressures of 24 to 35 MPa and temperatures of 580 °C to 610 °C.[1–5] Heat treatment of these steels consists of normalizing at a temperature of ~ 1050 °C and tempering at 720 °C to 780 °C. Under normalizing, the austenite transforms to lath martensite with a body-centered cubic (bcc) structure. Martensite has a four-level hierarchy in its morphology, *i.e.*, prior austenite grains (PAGs) are divided into packets, blocks, and laths with a high dislocation density in the lath interiors.[6] Tempering leads to the precipitation of $M_{23}C_6$ carbides and M(C,N)-type carbonitride particles.

$M_{23}C_6$ carbides with sizes of 60 to 100 nm are precipitated mainly on the boundaries of PAGs, packets, blocks, and laths and M(C,N)-type carbonitride particles are distributed uniformly throughout the matrix. The microstructure after tempering is usually called a tempered martensite lath structure (TMLS) because the characteristic morphology of martensite is retained after tempering owing to the precipitation of $M_{23}C_6$ carbides and M(C,N)-type carbonitrides that exert high Zener drag forces on the PAG boundaries, packets, blocks, and lath boundaries and serve as effective barriers to dislocation motions.

The superior creep resistance of these steels is attributed to three factors. First, the TMLS contributes to an increase in strength owing to internal stresses inherent in martensite.[1,2,6–11] Second, dispersion strengthening is provided by nanoscale boundary $M_{23}C_6$ carbides and fine M(C,N)-type carbonitrides homogeneously distributed in the lath interiors.[1,7,9,12–14] Third, solution strengthening is attributed to Cr, Co, Mo, and W solutes in a ferritic matrix.[1,13,15,16] Martensitic steels with Cr ranging from 9 to 10.5 wt pct are tough in tempered conditions.[17–26] For instance, the impact toughness of P91 and P92 steels at room temperature is 180 and 250 J, respectively.[22,25] However, additional alloying by substitutional solids, and lowering N and increasing B, may decrease the fracture toughness.[24]

About 50 years ago, 12 Cr steels were introduced in service for high-temperature rotors and blades of steam turbines operating up to 565 °C.[1] At present, a new generation of these steels with improved creep strength providing service at temperatures up to 650 °C has been developed.[1] The fracture toughness of these steels is a critical property for their application as structural materials for rotating turbine parts and components.[1] The fracture toughness required for a turbine application must be at a level of 70 MPa $\times$ $m^{0.5}$ or higher.[27,28]

J. BORISOVA, V. DUDKO, R. MISHNEV, and R. KAIBYSHEV are with the Belgorod State University, Pobeda 85, Belgorod, Russia, 308015. Contact e-mail: valeriy_dudko@yahoo.com
Manuscript submitted November 5, 2018.
Article published online May 20, 2019

However, an increase in Cr content results in deterioration of the fracture toughness at ambient temperature and an increase in the ductile-to-brittle transition temperature (DBTT) of the steel.[24,29] In addition, aging during service leads to a two- to four-fold decrease in the Charpy V-notch impact energy at ambient temperature, and strongly increases the DBTT owing to the precipitation of the Laves phase.[18,19,26] However, the effect of the Laves phase on the impact toughness has not been studied in sufficient detail.[18,30–33]

The aim of the present study is to examine the DBT in a novel 12 pct Cr steel modified with 4 pct Co and 0.8 pct Cu. Specific attention is paid to the mechanism responsible for the DBT. In addition, the effect of aging at 650 °C on the fracture toughness is evaluated to establish the mechanism of embrittlement attributed to the Laves phase.

II. EXPERIMENTAL

Steel with a chemical composition of Fe-0.1C-11.9Cr-4.0Co-0.8Cu-0.59Mo-2.2W-0.22V-0.05Nb-0.065Ni-0.05 Si-0.05Mn-0.008B-0.012 N (in mass pct) was fabricated by the Central Research Institute for Machine-Building Technology, Moscow, Russia. This steel was normalized at 1070 °C for 40 minutes and then tempered at 770 °C for 3 hours. Aging was carried out at a temperature of 650 °C for 643 hours. Standard Charpy V-notch specimens with a 10 × 10 mm^2 cross section, 55-mm length, and 2-mm V-notch were tested using an Instron 450 J impact machine (Model SI-1M) with an Instron Dynatup Impulse data acquisition system following the ASTM E-23 standard at temperatures ranging from − 20 °C to 200 °C. The percent of shear fracture was measured in accordance with the ASTM E-23 standard.[34]

Structural characterizations were carried out using a JEM-2100 (JEOL Ltd., Tokyo, Japan) transmission electron microscope (TEM) and a Quanta 600 FEG scanning electron microscope (SEM) (FEI Corporation, Hillsboro, OR). Chemical compositions of secondary phases were measured by scanning TEM (STEM) in conjunction with an INCA energy dispersive X-ray spectroscope (EDX) (Oxford Instruments, Oxfordshire, UK). The surface of the specimens for SEM observation was mechanically polished and then electropolished using a solution of 10 pct perchloric acid in glacial acetic acid. TEM foils were prepared from 3-mm disks, which were mechanically ground and polished down to about 0.1 mm. Then, a standard double-jet electropolishing procedure with a aforementioned solution was used to obtain electron transparent holes in the foils. The electropolishing was performed at room temperature and voltages of 25 V. Extraction replicas were prepared by etching the polished surface of the specimen in 4 pct solution of HNO_3 followed by the evaporation of carbon onto a polished and etched surface. Then, the metallic matrix was dissolved in 10 pct HCl with ethanol at a voltage of 2 V. The small squares of carbon extraction replicas were captured using copper grids.

The lath/subgrain sizes were measured using TEM micrographs by the linear intercept method, including all clearly visible (sub)boundaries. The dislocation densities were evaluated by counting the individual dislocations in the grain/subgrain interior, and each data point represented at least six arbitrarily selected representative TEM images.

The sizes of dimples/voids on the fracture surface were calculated using SEM micrographs by measuring the major and minor axes of more than 1500 clearly visible voids. The aspect ratio was estimated as the ratio of the highest dimension of a cavity to that in the perpendicular direction.

The equilibrium volume fractions of the precipitated phases in the present 12 pct Cr steel at tempering and aging temperatures of 770 °C and 650 °C, respectively, were calculated by Thermo-Calc software (Ver. 5) using the TCFE7 database.

III. RESULTS

A. *Microstructure After Tempering*

The microstructure of the steel after normalizing and tempering is shown in Figure 1. The structural parameters and characteristics of $M_{23}C_6$ carbides are summarized in Table I. In Figure 2 the microstructural parameters revealed in the current work are plotted with data for the other 9 to 12 pct Cr steels[10,22,23,25,35–41] for comparison.

The size of the PAGs is 38 ± 8 μm, and the average distance between high-angle boundaries (HABs) revealed by an orientation imaging microscopy (OIM) is 6.6 ± 4 μm (Figures 1(a) and (b)). TMLS of the present steel is characterized by an increased PAG size and HAB spacing as compared to other high-Cr steels (Figures 2(a) and (b)). On the other hand, a lath thickness of 286 ± 58 nm corresponds well to the other steels containing 9 to 10.5 wt pct Cr[10,22,23,26,36,41] (Figure 2(c)). A dislocation density of ~ (2.2 ± 0.9) × 10^{14} m^{-2} within the lath interiors in the present 12 pct Cr steels and steels containing 9 to 10.5 wt pct Cr is nearly the same[10,23,35–37,40,41] (Figure 2(d)).

Another feature of the TMLS of the modified 12 pct Cr steel is the presence of δ-ferrite, whose volume fraction is 3.8 pct. It is worth noting that the presence of δ-ferrite is a characteristic feature of 12 pct Cr steels.[41,42]

Generally, the chemical composition of 9 to 12 pct Cr steels contains elements that stabilize the austenite and ferrite phases. Balance between the ferrite and austenite-stabilizing elements should be provided in order to avoid δ-ferrite formation during normalizing. However, thermodynamic equilibrium calculations cannot accurately predict the formation of δ-ferrite. The δ-ferrite might remain in the steel as a non-equilibrium phase because diffusion transformation of the δ-ferrite to austenite requires much more time than cooling of castings to room temperature. The dissolution of δ-ferrite during consecutive austenizing is a slow process, and this may leave δ-ferrite in the steel. The susceptibility to

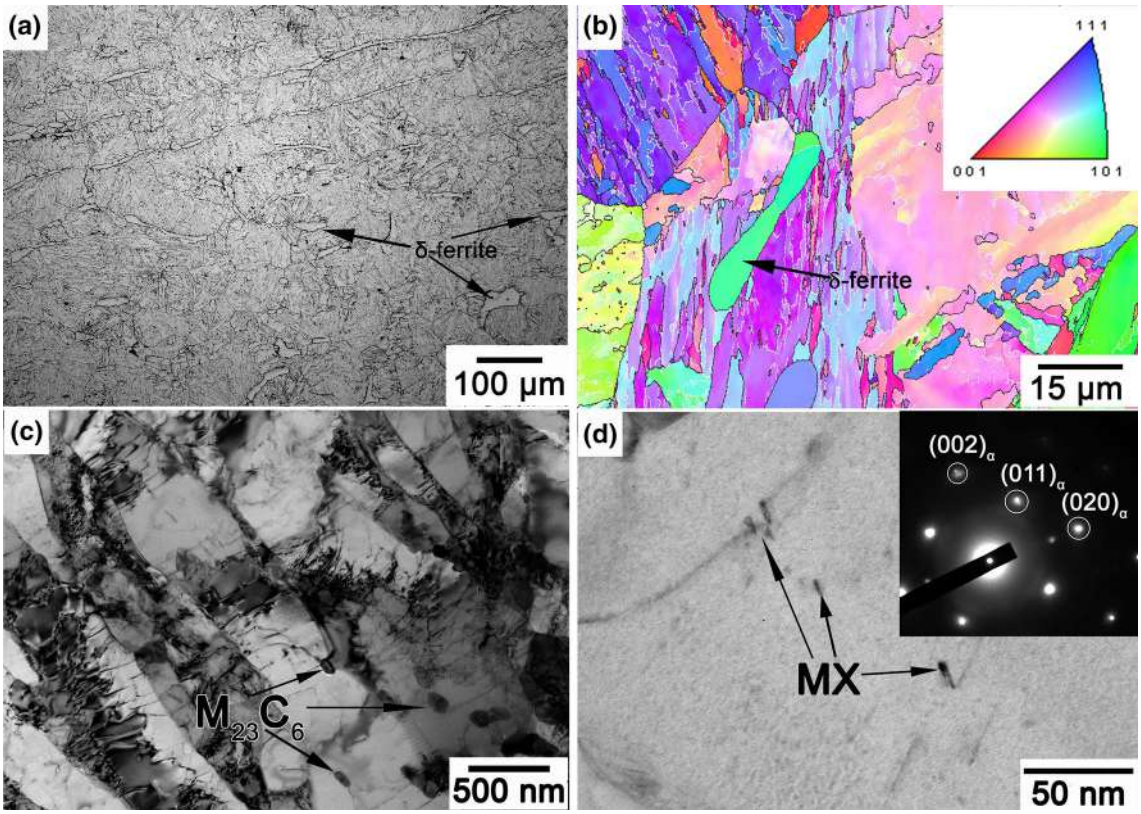

Fig. 1—Microstructure of 12 pct Cr steel after tempering at 770 °C for 3 h: (*a*) optical micrograph, (*b*) OIM map, (*c*) TEM micrograph of tempered martensite lath structure, and (*d*) MX carbonitrides within laths.

Table 1. Structural Parameters After Tempering and Aging

Condition	Volume Fraction of Particles, F_{VB} (Pct)	Mean Size of Particles (nm)	Lath Width (nm)	Density of Particles, β (μm^{-1})	Volume Fraction of Voids in the Stable Crack Propagation Zone (Pct)
Tempering					
$M_{23}C_6$	2.15	83 ± 36	286 ± 58	0.85	0.70
Aging					
$M_{23}C_6$	2.25	83 ± 36	371 ± 90	0.98	1.86
Laves phase	1.76	160		0.22	
«Cu»	< 0.49	< 75		0.31	

forming δ-ferrite can be estimated by a Cr-equivalent value that depends on the chemistry of the material and is given as follows[43,44]

$$\begin{aligned} \text{Cr}-\text{eq} \;=\; & \text{Cr} + 0.8\,\text{Si} + 2\,\text{Mo} + 1\,\text{W} + 4\,\text{V} \\ & + 2\,\text{Nb} + 1.7\,\text{Al} + 60\,\text{B} + 2\,\text{Ti} \\ & + 1\,\text{Ta} - 2\,\text{Ni} - 0.4\,\text{Mn} - 0.6\,\text{Co} \\ & - 0.6\,\text{Cu} - 20\,\text{N} - 20\,\text{C}\ (\text{pct}) \end{aligned} \quad [1]$$

It was experimentally revealed[43,44] that δ-ferrite will not be present if the Cr-eq is less than 10. The Cr-eq value calculated for the modified 12 pct Cr steel in accordance with Eq. [1] is 11.6. Therefore, the formation of δ-ferrite can be expected.[43,44] Grains of δ-ferrite with nearly equiaxed and elongated shapes appear at the PAG boundaries and along the packet boundaries, respectively (Figures 1(a) and (b)).

The dispersion of the secondary phases consists of MX carbonitrides located within the lath interiors and boundary $M_{23}C_6$ carbides (Figures 1(c) and (d), 3, 4(b) and (d)). The carbonitrides obey the Baker-Nutting orientation relationship, *i.e.*, $(100)_{VC} \parallel (100)_\alpha$, $[011]_{VC} \parallel [001]_\alpha$, and are enriched by V (Figures 1(d) and 3(d)). Two types of MX dispersoids can be distinguished by their shapes. The first type is particles with platelike shapes and average longitudinal and

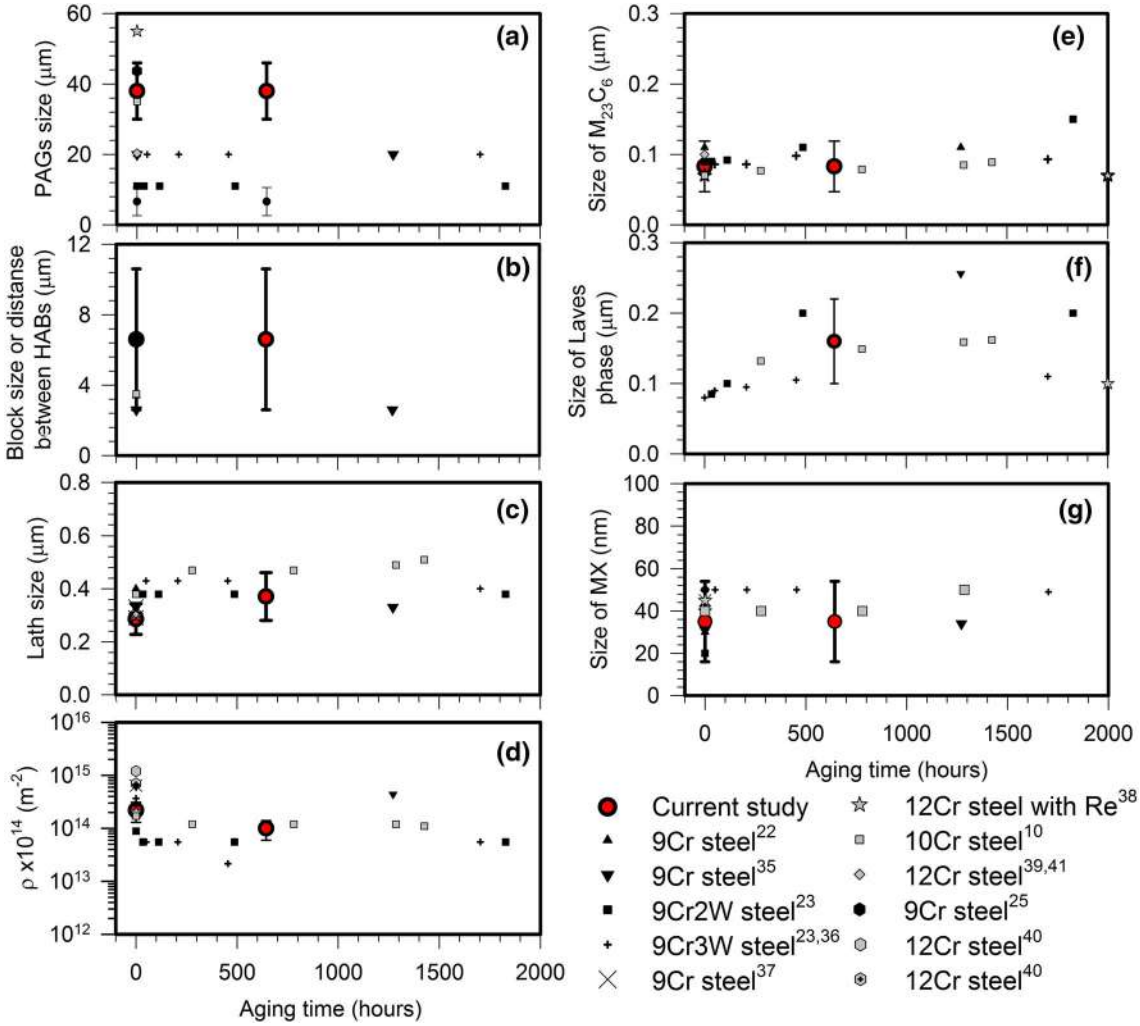

Fig. 2—Comparison of experimental parameters of microstructure after tempering at 720 °C to 770 °C followed by aging at 650 °C with literature data: (*a*) dependence of PAG size on aging time, (*b*) dependence of block size or distance between HABs on aging time, (*c*) dependence of lath size on aging time, (*d*) dependence of dislocation density ρ on aging time, (*e*) dependence of $M_{23}C_6$ carbide size on aging time, (*f*) dependence of Laves phase particle size on aging time, and (*g*) dependence of MX carbonitride size on aging time.

thickness dimensions of ~ 10 and ~ 4 nm, respectively (Figure 1(d)). The second type of particles is MX carbonitrides with equiaxed shapes and an average size of ~ 35 nm (Figures 3(a) and (d)). The size (Figure 2(g)) and orientation relationship of carbonitrides as revealed in the present study correspond well to data reported for 12 pct Cr creep-resistant steels by other studies.[41,42,45,46]

The $M_{23}C_6$ carbides are enriched by Cr, and their average size is 83 nm. Assuming that carbides precipitate uniformly at all types of TMLS boundaries, the particle density can be estimated as follows[11,24,47]:

$$\beta = \frac{3DF_{v\mathrm{B}}}{\pi d^2} \qquad [2]$$

where F_v is the particle volume fraction, D is the size of the smallest structural element (*i.e.* the lath thickness), and d is the size of the particles. The calculated particle densities are listed in Table I. The densities of these boundary carbides are lower than in the 10.5 pct Cr steel and higher than in P92-type steel.[24]

It should be noted that most $M_{23}C_6$ carbides precipitate on HABs of PAGs, packets, and blocks, and look like chains along these boundaries in 12 pct Cr steel (Figures 1(c), 3(a) through (c), 4(b) and (d). $M_{23}C_6$ carbides on interlath boundaries are rarely observed.

Therefore, the particle density of HABs in 12 pct Cr steel is higher than that listed in Table I. Another feature of TMLS of 12 pct Cr steel is dense precipitations of $M_{23}C_6$ at the boundaries of δ-ferrite (Figure 4(a)). Thermo-Calc calculations revealed that the mass fractions of carbon in the δ-ferrite and austenite at 1150 °C are 2.1×10^{-4} and 9.8×10^{-4}, respectively. Thermo-Calc predicted a lack of δ-ferrite at 1070 °C. It is obvious that the difference in carbon concentrations between the δ-ferrite and martensite phases after cooling remains the same as between δ-ferrite and austenite at 1150 °C. Therefore, the carbon concentration in the martensite phase is about five times higher than that in the δ-ferrite phase. The difference in the nominal carbon concentrations of the δ-ferrite and martensite phases increases the driving force for interdiffusion.[48] Thus, the enhanced diffusion of carbon

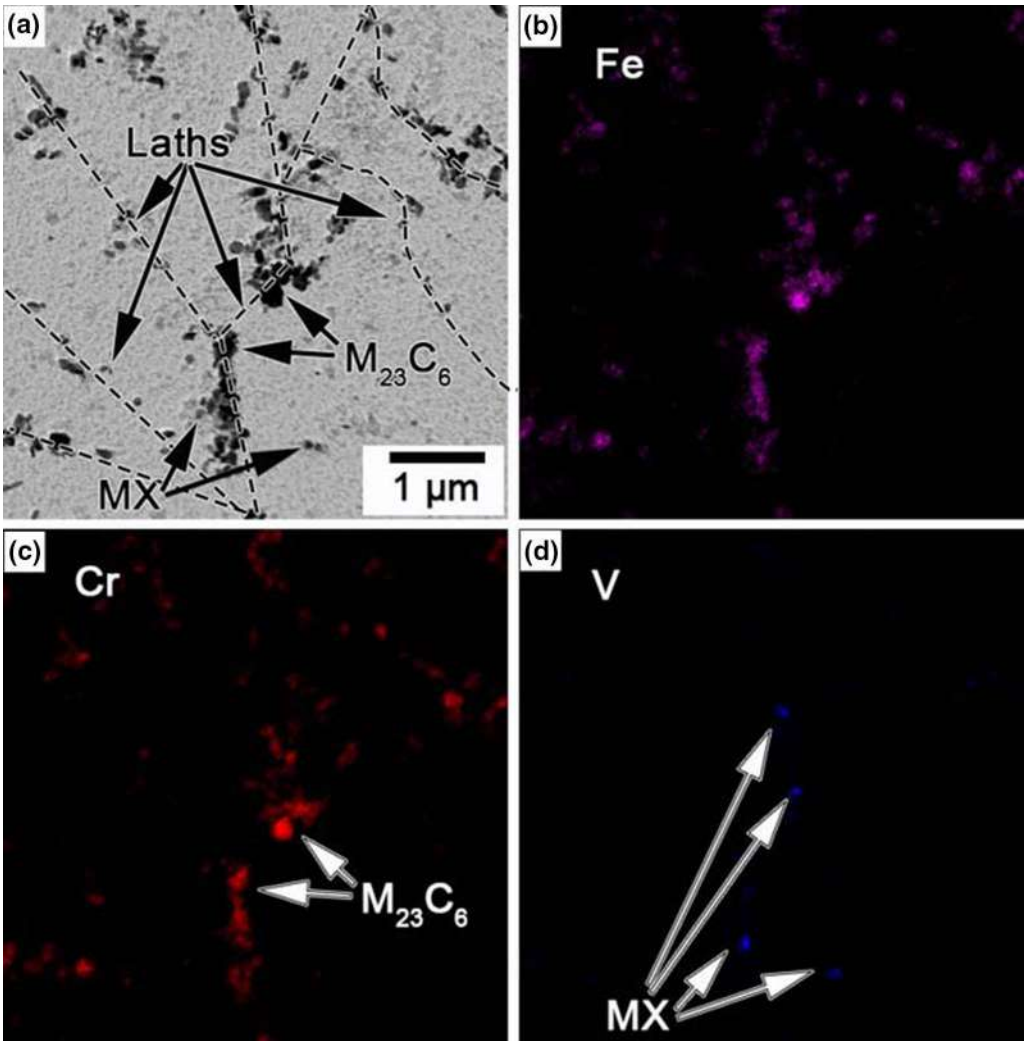

Fig. 3—STEM/EDX elemental mapping of carbon extraction replica with precipitates in 12 pct Cr steel after tempering at 770 °C for 3 h: (*a*) STEM micrograph and EDX elemental mapping showing (*b*) Fe-reach, (*c*) Cr-reach, and (*d*) V-reach areas.

from the martensite phase to the ferrite phase facilitates the precipitation and growth of boundary carbides during tempering.

B. *Microstructure After Aging*

The microstructure evolved by aging at a temperature of 650 °C for 643 hours is shown in Figures 4(c), (d), and 5. The microstructural parameters are presented in Table I. The mean distance between HABs does not change by aging (Figure 5(a)). By contrast, lath coarsening occurs because of low Zener drag pressure associated with the particles precipitated on the lath boundaries.[10,11,35,49] The average lath size increases to 371 nm and the dislocation density decreases to 10^{14} m^{-2} during the aging (Figures 2(c) and (d)). The dispersion of MX carbonitrides remains almost unchanged during the aging (Figures 2(g) and 5(e)).

The average size of $M_{23}C_6$ carbides does not depend on the aging (Table I, Figure 2(e)). Additional precipitations of $M_{23}C_6$ carbides were suggested by Thermo-Calc calculations (Table I). The main changes in the dispersion of secondary phases are associated with the precipitation of Laves phase particles with an average size of 160 nm. These particles nucleate at $M_{23}C_6$ carbide/ferrite interfaces (Figures 4(d) and 5(c)) and the boundaries of blocks, δ-ferrite, and laths (Figures 4(c), 5(b), and (e)).

Continuous chains of $M_{23}C_6$ carbides and Laves phase particles evolve on the boundaries of PAGs, packets, and δ-ferrite (Figure 4(c)), whereas discontinuous chains are observed on the boundaries of blocks and laths (Figures 4(b) and 5(b)).

Particles with a length of 573 nm and a thickness of 68 nm nucleate at δ-ferrite boundaries and grow to δ-ferrite interiors (Figures 5(d) and (f)). An EDX analysis of carbon replicas (Figure 5(f)) identifies this phase as the χ-phase ($Fe_{36}Cr_{12}W_{10}$) that is usually observed in high-chromium ferritic steels.[50]

Thermo-Calc calculations predicted the precipitation of Cu particles with a volume fraction of 0.49 pct from solid solution at a temperature of 650 °C (Table I). Numerous holes are observed at lath boundaries and block boundaries (Figures 5(b) and 6(a)). These holes

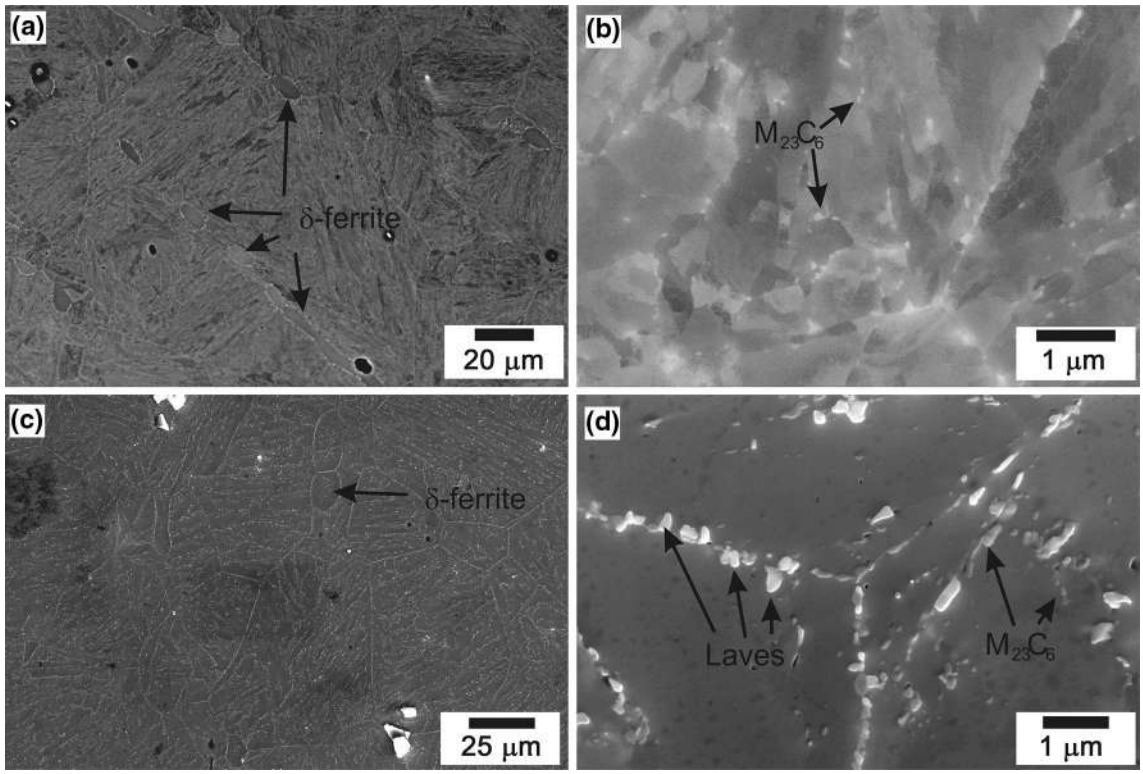

Fig. 4—SEM micrographs obtained by backscattered electrons after (*a*, *b*) tempering at 770 °C for 3 h and (*c*, *d*) after aging at 650 °C for 643 h.

are considered to be footprints of Cu particles. It is known that the addition of Cu to high-chromium steels results in the formation of Cu particles that are distributed at boundaries of PAGs, packets, blocks, laths and lath interiors.[51,52] However, in the present study, Cu dispersoids were found on lath boundaries and the boundaries of blocks only (Figure 6). Since the Cu particles are quickly dissolved by the electropolishing, the holes appear at sites of Cu particles. The average diameter of the holes is 75 nm. Therefore, the mean size of the Cu particles should be smaller than this value. The average size of the Laves phase particles in the present 12 pct Cr steel corresponds well to that obtained in other high-Cr steels[10,23,35,39] (Figure 2(f)). In addition to equiaxed Laves phase particles, small regions with almost-continuous chains of Laves phase particles along the boundaries are observed. Figures 6(b) and (c) show the TEM/EDX elemental mapping of the regions with the film-like and equiaxed particles of the Laves phase. The precipitation of the Laves phase and Cu particles leads to an increase in the particle density calculated by Eq. [2] at the boundaries of TMLS by a factor of 1.8 (Table I).

C. *Impact Tests*

The temperature dependence of the Charpy V-notch impact energy for the 12 pct Cr steel in tempered and aged conditions is shown in Figure 7. The lower shelf region of the tempered steel is located below 0 °C, whereas the transition region is observed at temperatures ranging from 0 °C to 100 °C and the upper shelf region is located above 100 °C. The DBTT of the tempered steel, calculated as the temperature corresponding to the impact energy absorption halfway between the upper and lower shelf energies of the steel, is 41 °C. The value of the upper shelf energy is 250 J/cm^2.

At room temperature below the DBTT, the tempered steel possesses a high value of absorbed energy of 110 J/cm^2, although at 0 °C the absorbed energy falls to 9 J/cm^2. Full embrittlement takes place at a relatively high temperature, which is higher than that for the 10.5 pct Cr steel with low N and high B by 80 K[24] and a P92-type steel by 190 K.[22] Therefore, increasing the Cr content from 10 to 12 wt pct along with increasing the Co content from 3 to 4 wt pct along with an addition of 0.8 wt pct Cu significantly deteriorates the fracture toughness.

The aging results in a shift in the temperature dependence of the Charpy V-notch impact-absorbed energy to higher temperatures (Figure 7). The lower shelf region of the aged steel is located at temperatures below 20 °C, the transition region is observed at temperatures from 20 °C to 150 °C, and the upper shelf region is located at temperatures above 200 °C. The DBTT increases to 122 °C. The upper shelf energy for the aged steel is 230 J/cm^2, which is slightly lower than that in the tempered steel. At room temperature, the aging results in a five-time reduction in the fracture toughness of the 12 pct Cr steel down to 20 J/cm^2. At 0 °C, the Charpy V-notch impact toughness is 8 J/cm^2. The degradation in the fracture toughness caused by

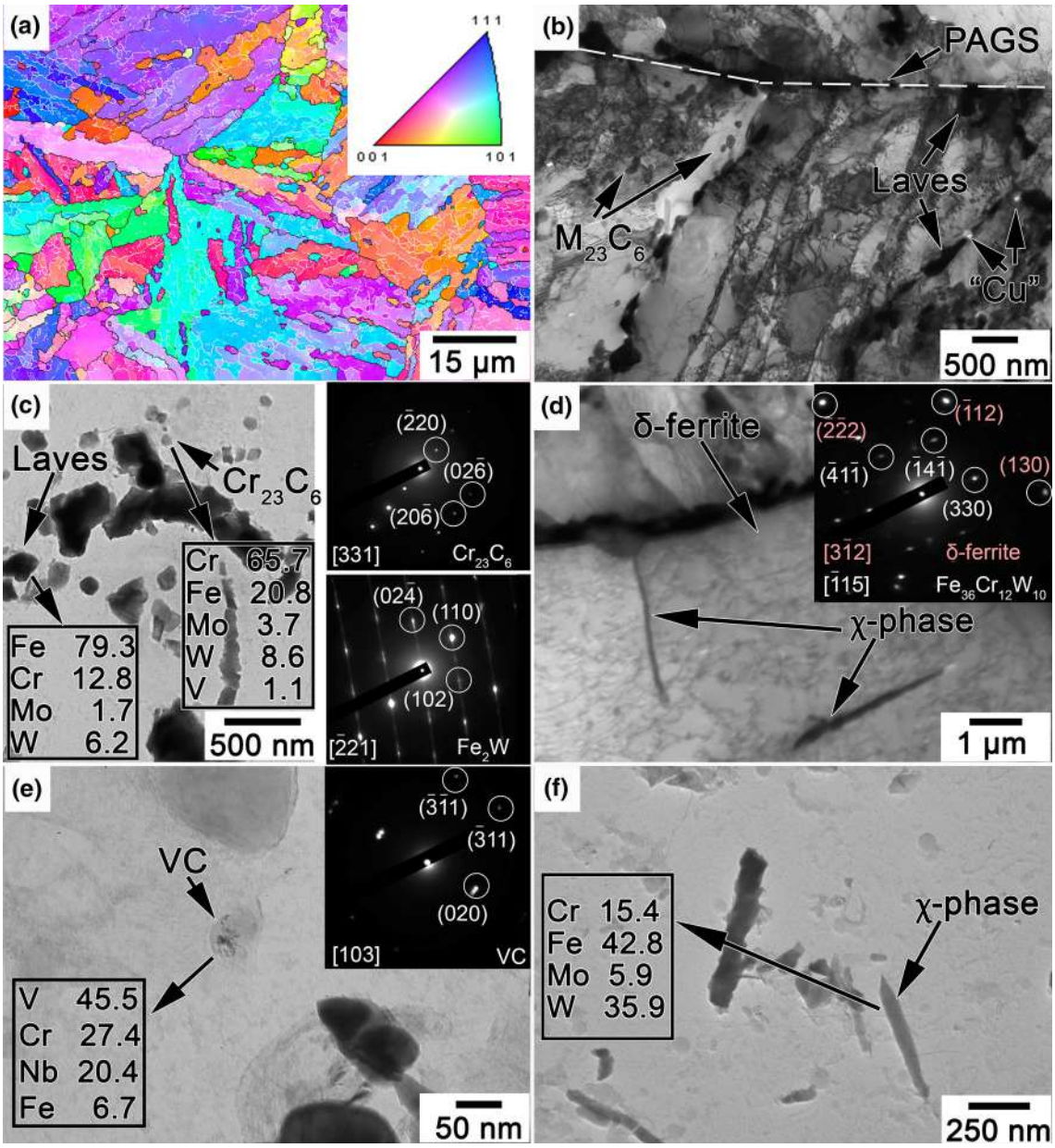

Fig. 5—Microstructure after long-term aging at 650 °C for 643 h: (*a*) OIM map with martensite packets and blocks, (*b*) TEM micrograph of martensite laths, (*c*) typical precipitates on carbon replica, (*d*) TEM micrograph of δ-ferrite grain with coarse elongated χ-phase particles, (*e*) MX carbonitride particle on carbon replica, and (*f*) χ-phase particles on carbon replica.

aging is more pronounced in this steel than in other high-Cr steels.[18,20,26,33,53,54]

Figure 8 shows a series of load-*vs*-deflection and absorbed energy-*vs*-deflection curves derived from the recorded impact tests of tempered steel. The characteristic points of the general yield load (P_{GY}), maximum load (P_m), fast fracture load (P_F), and arrest load (P_A) are shown. It is known[22,24,55–57] that the onset of crack initiation occurs between the P_{GY} and P_m points, stable crack propagation occurs from the P_m to P_F points, unstable crack propagation occurs from the P_F to P_A points, and shear lips form beyond the P_A point.

The area under the load-deflection curve up to point P_m represents the fracture initiation energy E_i, while the remaining area represents the fracture propagation energy E_p. The calculated values for E_i and E_p are listed in Table II. It is seen that at the lower shelf and DBT regions, the E_i and E_p values are nearly the same; while at the upper shelf, the energy of crack propagation becomes significantly higher than the energy of crack initiation.

An analysis of the load-deflection curves reveals that the tempered 12 pct Cr steel (Figure 8(a)) exhibits a fully ductile mode of fracture with a total energy of 160 to 250 J at $T \geq 100$ °C. The impact energy is effectively absorbed under stable crack propagation (Figure 8, Table II). At 50 °C, well-defined P_A and P_F points appear. Stable crack propagation takes place from the P_m to P_F character points, results in a relatively high deflection of 3

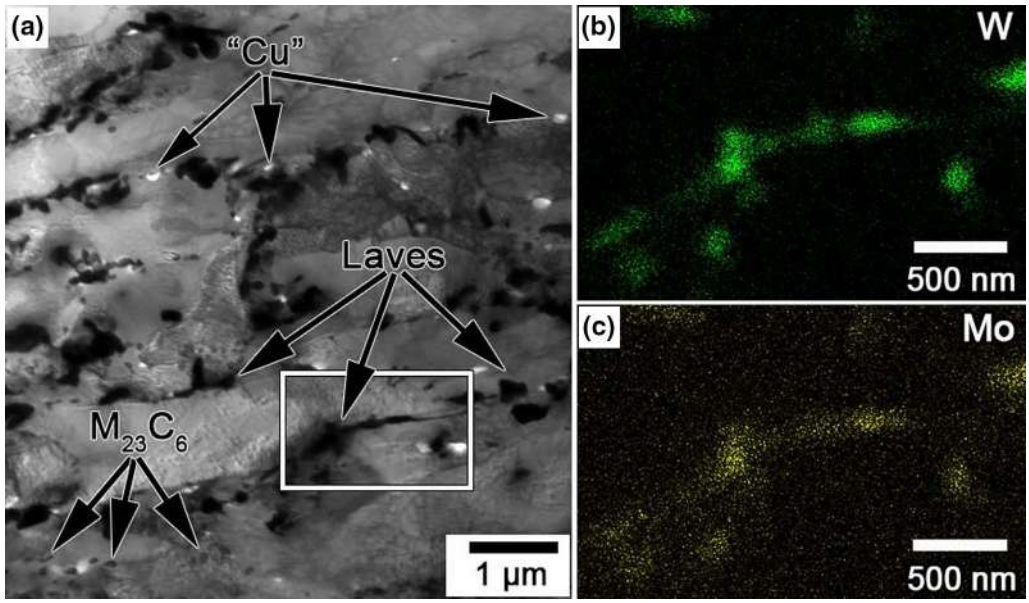

Fig. 6—Typical precipitates at lath boundaries and boundaries of blocks after aging at 650 °C for 643 h: (*a*) STEM microstructure and (*b*, *c*) STEM/EDX elemental mapping of framed region in (a).

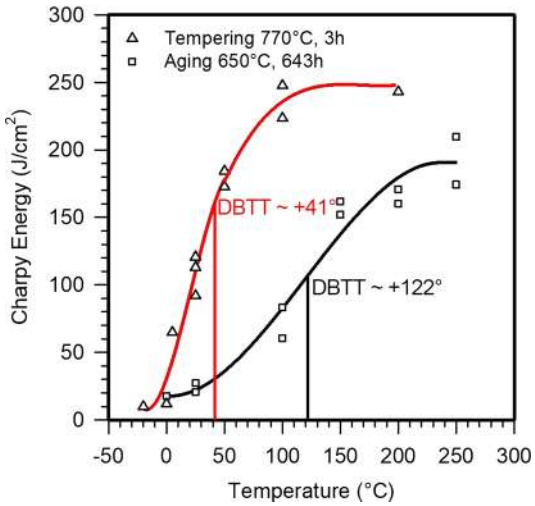

Fig. 7—Temperature dependence of Charpy energy for 12 pct Cr steel after tempering and aging.

mm, and therefore occurs in a ductile manner (Figure 8). Crack propagation between points P_F and P_A occurs with negligible deflection; therefore, stable crack propagation is replaced by unstable crack propagation in a brittle manner at point P_F (Figure 8). At point P_A, the unstable crack propagation is arrested, and the formation of shear lips by a ductile mechanism takes place. The area under the fracture diagram between points P_F and P_A corresponds to the impact energy consumed by unstable crack propagation and is negligibly small because of the cleavage crack propagation mechanism.

The total fracture energy is mostly consumed during the initiation of the crack with critical dimensions and the stage of stable crack propagation. It should be noted that the values of E_i are the same at temperatures from 20 °C to 200 °C (Table II). A decrease in the test temperature from 100 °C to 20 °C shortens the stage of stable crack propagation, causing a large decrease in the impact-absorbed energy. At room temperature, unstable crack propagation occurs without crack arrest at point P_A and additionally decreases the absorbed impact energy. A further decrease in the test temperature leads to the disappearance of the stable crack propagation zone, and the fracture toughness corresponds to an impact energy of 1 to 5 J that is consumed only during the crack initiation stage.

At 0 °C, the load for the onset of unstable crack propagation in the tempered steel is twice that of the steel subjected to aging, although the Charpy V-notch adsorbed energies of these two conditions are nearly the same. Therefore, aging decreases the load for the onset of unstable crack propagation.

The impact behavior of the 12 pct Cr steel subjected to aging is quite different (Figure 8(b)). Embrittlement occurs at much higher temperatures than in the tempering condition. The aged specimens exhibit fully ductile fracture behavior at $T \geq 200$ °C. The unstable crack propagation stage takes place even at 150 °C, while steel absorbs a relatively high impact energy of 150 J/cm^2. Decreasing the temperature to 100 °C significantly shortens the stable crack propagation stage and correspondingly decreases the absorbed energy to 69 J/cm^2 (Table II). At room temperature, the stable crack propagation stage is not observed and the impact energy of 25 J/cm^2 is attributed to the energy absorption during the crack initiation stage.

D. *Fractography*

Low- and high-magnification SEM images of the fracture surfaces of Charpy impact specimens in tempered and aged conditions are shown in Figures 9, 10, and 11. The sizes of the fracture zones and percentages of

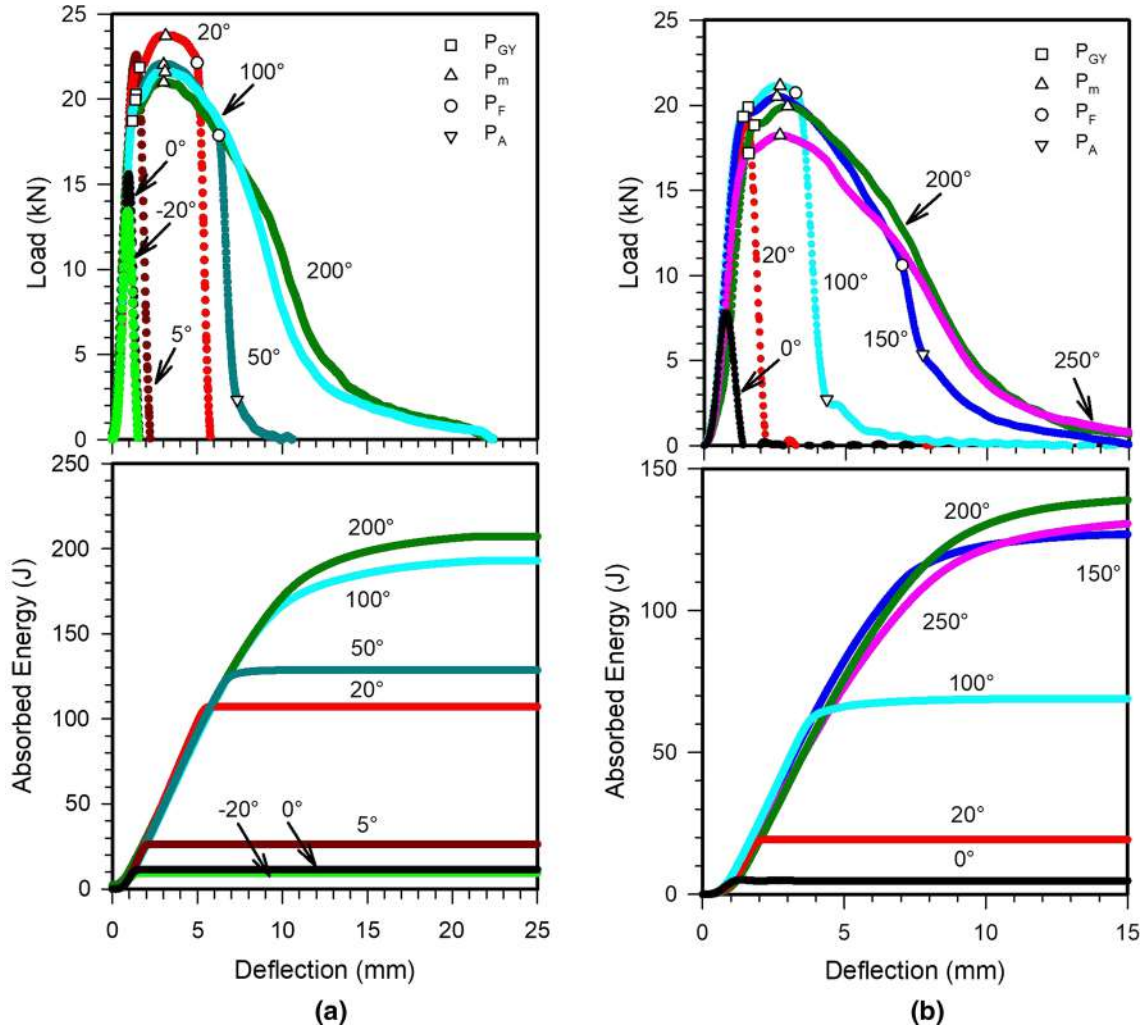

Fig. 8—Load-deflection and absorbed energy deflection curves for 12 pct Cr steel after (*a*) tempering and (*b*) aging.

Table II. Dynamic Parameters Calculated from Load-Deflection Curves

	Tempered Condition		Aged Condition	
Temperature (°C)	Fracture Initiation Energy E_i (J)	Fracture Propagation Energy E_P (J)	Fracture Initiation Energy E_i (J)	Fracture Propagation Energy E_P (J)
− 20	5	4	—	—
0	6	5	5	0
5	16	11	—	—
20	54	52	19	0
50	49	80	—	—
100	50	143	38	31
150	—	—	35	92
200	52	156	36	104
250	—	—	35	95

the shear fracture area are listed in Table III. An inspection of Table III and Figure 7 shows that the fracture appearance transition temperature (FATT) corresponding to the equal fractions of the brittle and ductile fracture surfaces[34] coincides with the DBTT after both tempering and aging, as in the other high-Cr steels.[24,58]

The results of a fractography study explain the data obtained from an instrumented Charpy V-notch test. A fully ductile fracture corresponds to the upper shelf region of the DBT diagram (Figure 7). The fraction of ductile fracture is 100 pct at temperatures of 100 °C and 200 °C in the tempered and aged conditions, respectively

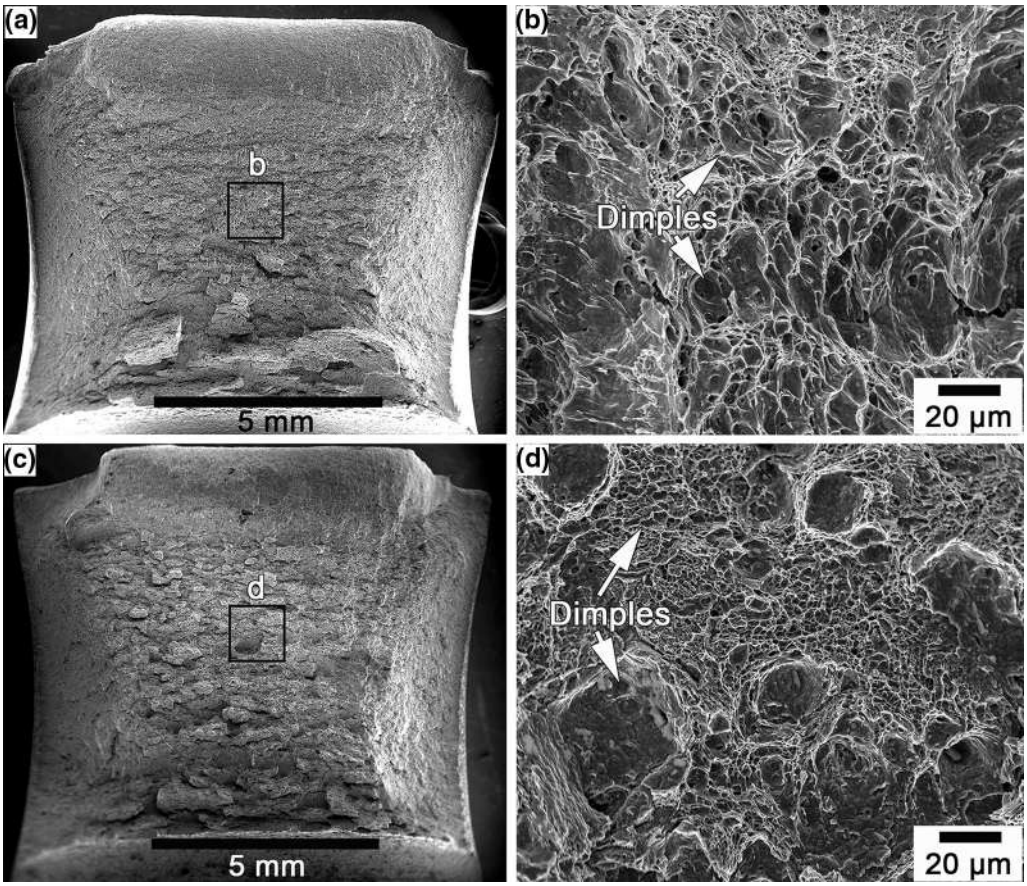

Fig. 9—Fracture surface of Charpy V-notch specimen of 12 pct Cr steel after tempering at 770 °C and testing at 100 °C: (*a*) general view and (*b*) high magnification of indicated portion. Fracture surface after aging at 650 °C for 643 h and testing at temperature of 200 °C: (*c*) general view and (*d*) high magnification of indicated portion.

(Figures 9(a) and (c)). The fracture surfaces are characterized by dimpled transgranular fractures resulting from the coalescence of microvoids (Figures 9(b) and (d)).

Figure 10 shows typical fracture surfaces of tempered and aged specimens in the region of the DBT. Four specific character zones[56,59] (zone of crack initiation, zone of stable crack propagation, zone of unstable crack propagation, and shear lip zones) are distinguished in the tempered and aged specimens (Figures 10(a) and (b)). However, aging significantly decreases the fraction of shear fractures (Figures 10(a) and (b) and Table III).

The stable crack propagation zone in the tempered specimen is characterized by the alternating the fine dimples with size of ~ 0.6 to 1 μm and coarse dimples with size of ~ 6 to 20 μm (Figure 10(1a)). Second phase particles are occasionally observed at the bottom of the coarse dimples, suggesting microvoid nucleation.[60] An analysis of dimple size distribution in the stable crack propagation zones (Figure 11(a)) shows that aging leads to an increased fraction of fine dimples with dimensions ranging from 0.6 to 1 μm by ~ 12 pct. The average size of the dimples in tempered specimens is 1.5 times higher than that in aged specimens. The area of the fracture surface occupied by the fine dimples increases from ~ 20 pct after tempering to ~ 40 pct in the aged specimen (Figure 11(b)). The average value of the aspect ratio is 1.7 to 2.7 for both the tempered and aged specimens.

A high value of the aspect ratio indicates that micro-cracks evolve at the boundaries. Plastic deformation and the coalescence of micro-cracks lead to the formation of elongated dimples along the boundaries. The size of the dimples on a fracture surface is governed by the number of microvoids that nucleate in the zone of plastic deformation ahead of the crack tip. A longer distance between the nucleation sites of microvoids lets them to grow to a larger size. A decrease in distance between nucleation sites owing to precipitation of the Laves phase during long-term aging promotes the coalescence of microvoids.[61] Therefore, the precipitation of the Laves phase during aging significantly increases the number of nucleation sites of microvoids and decreases the dimple size.

The precipitation of the Laves phase facilitates a dimple fracture that decreases the upper shelf energy of the aged steel (Figure 7). A fracture in the unstable crack propagation zone after tempering and aging occurs by quasi-cleavage transgranular mechanisms (Figures 10(2a) and (2b)).

The unstable crack propagation zone, where the fracture occurs in quasi-cleavage manner,[22,24,60] expands while other zones shorten with decreasing

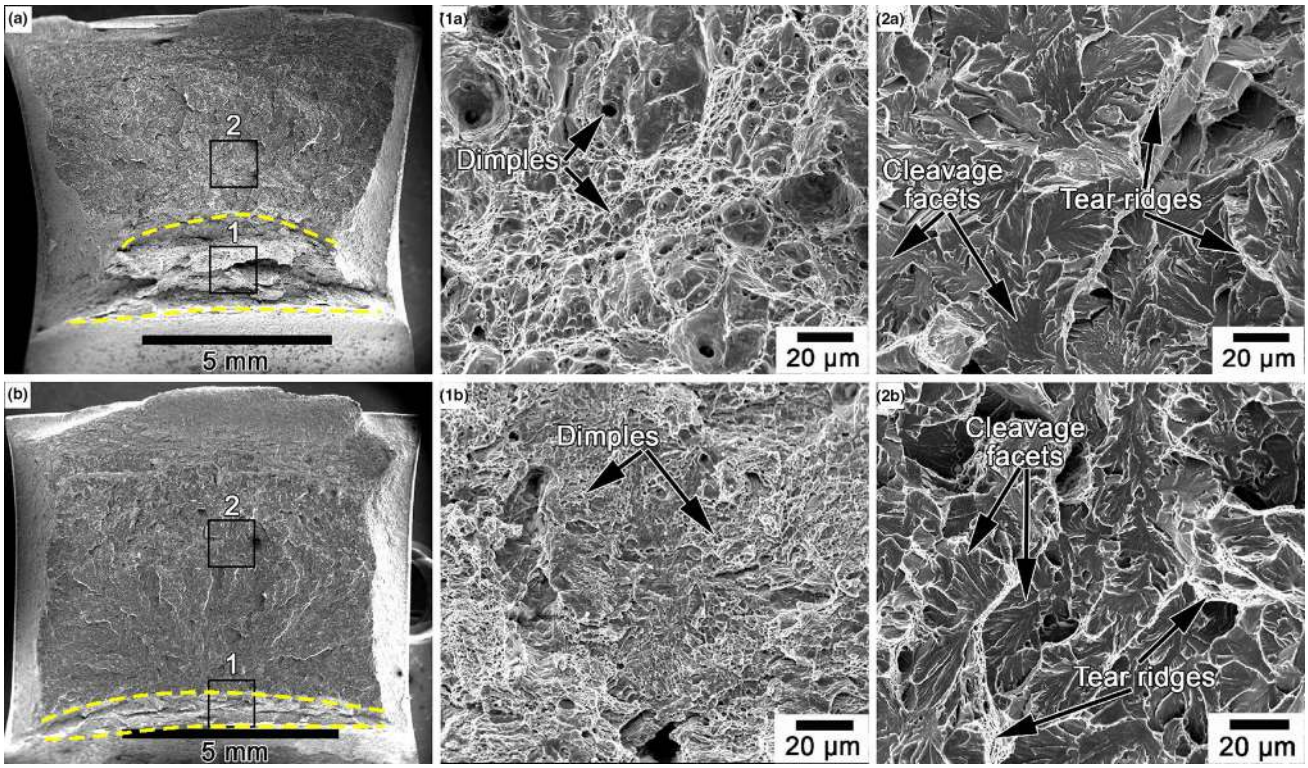

Fig. 10—Fracture surface of 12 pct Cr steel in long-term aged condition after impact tests at (*a*) 20 °C and (*b*) 100 °C. (1a, 1b) SEM micrographs showing high magnifications of ductile fracture in area framed by number 1 in (a) and (b). (2a, 2b) SEM micrographs showing high magnifications of quasi-cleavage fracture surfaces in area framed by number 2 in (a) and (b).

temperature (Table II). At the lower shelf region, the stable crack propagation zone and the shear lip zone were not detected in both the steel conditions (Figure 10).

At – 20 °C, the fracture surface of the tempered steel consists of a 150-μm crack initiation zone and an extended unstable crack propagation zone that supports the aforementioned analysis of the load-deflection curve. The fracture initiates without secondary crack formation (Figure 12(1a)) and propagates by the quasi-cleavage mechanism (Figure 12(2a)). Brittle fracture by the quasi-cleavage mechanism is accompanied by thin tear ridges with fine dimples of size ~ 0.3 to 1 μm (Figure 12(2a)).

At 20 °C, the fracture surface of the 12 pct Cr steel subjected to aging consists of a 264-μm crack initiation zone and 235-μm stable crack propagation zone (Figures 12(b) and (1b)). The presence of a short stable crack propagation zone causes an impact energy of 25 J/cm^2. However, the main fracture mechanism of aged steel in the lower shelf region is the same as that in the tempered steel, *i.e.*, a quasi-cleavage fracture with a small fraction of tear ridges (Figure 12(2b)). The fracture mechanisms in the unstable crack propagation zone in both tempered and aged conditions are almost the same. Thus, aging reduces the zones in which fractures occurs in a ductile manner and facilitates the onset of unstable crack propagation. This increases the DBTT and decreases the Charpy V-notch energy adsorbed in at the upper shelf region.

IV. DISCUSSION

The fracture toughness of the present 12 pct Cr steel modified with 4 pct Co and 0.8 pct Cu is relatively low. The steel exhibits DBT at 41 °C; full embrittlement takes place at 0 °C. Aging increases DBTT to 122 °C; unstable crack propagation may occur at $T \geq 100$ °C. However, the temperature of full embrittlement is the same after tempering and aging. It was recently shown[23,24] that the precipitation of film-like carbides of $M_{23}C_6$ or high-density chains of $M_{23}C_6$ along boundaries may significantly decrease the impact toughness of high-Cr martensitic steels.[23] Fedoseeva *et al.* showed that film-like carbides with an average thickness of approximately 50 nm resulted in intergranular fractures and a low value of the room temperature Charpy V-notch impact energy of 24 J/cm^2.[23] The replacement of film-like carbides of $M_{23}C_6$ by globular ones causes an increase in the room temperature Charpy V-notch impact energy to 206 J/cm^2. Mishnev *et al.*[24] showed that the formation of chains of $M_{23}C_6$ along the lath and block boundaries in a 10 pct Cr steel with low N and high B content decreases the Charpy V-notch impact energy in comparison with P92-type steel. As a result, the DBTT in the 10 pct Cr steel with low N and high B content was 73 K higher than in the P92 steel. Both works reported quasi-cleavage fractures at the low shelf of the DBT curve.[23,24] Therefore, the low fracture toughness at room temperature and high DBTT of the 12 pct Cr steel can be attributed to the formation of

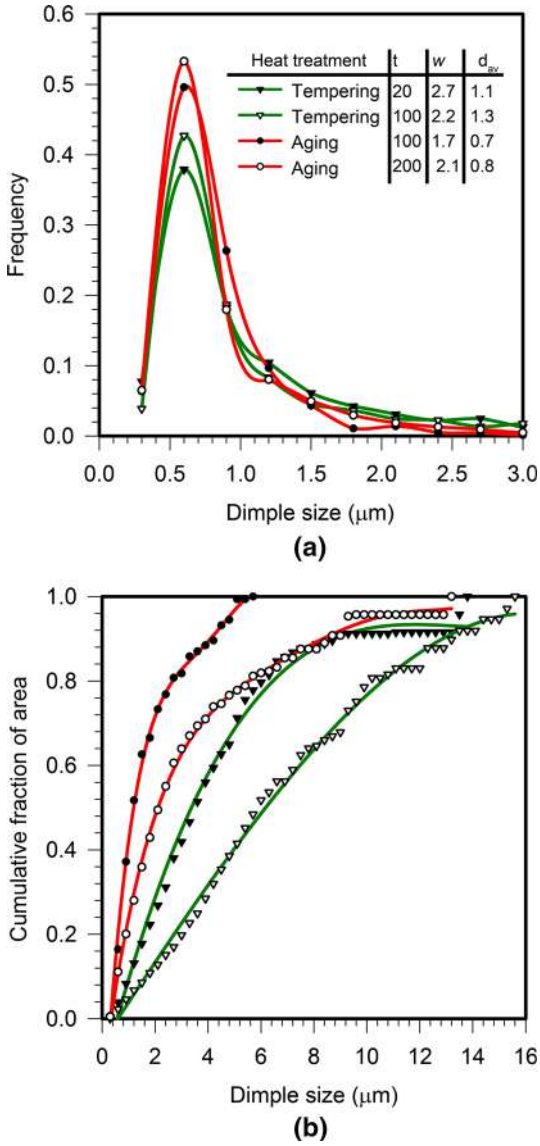

Fig. 11—(*a*) Dimple size distribution, their average aspect ratio *w*, and average size d_{av} at different impact test temperatures *t*. (*b*) Dependence of cumulative fraction of failure surface area occupied by dimples with particular size on dimple size.

semicontinuous or continuous chains of boundary particles, which promote fractures.

After tempering, the semicontinuous chains of $M_{23}C_6$ carbides appear on the boundaries of TMLS. Thus, a low DBTT can be attributed to the promotion of crack propagation by $M_{23}C_6$ carbide chains. This conclusion is supported by side views of the Charpy specimens of the tempered steels fractured at a temperature of 20 °C (Figures 13(a) and (b)). Continuous chains of voids evolve at carbide particles on the boundaries of PAGs, packets, and blocks. Coalescence of these cavities results in the formation of coarse voids visible at HABs (Figure 13(b)).

The preferential nucleation of voids at dispersion particles is in agreement with early studies.[62–65] Applied stress produces a uniform plastic strain in the matrix of dispersion-strengthened alloys. Precipitates deform only elastically because the strength of intermetallic particles is much higher than that of a matrix that induces long-range internal stress.[63] Therefore, dispersion particles serve as stress concentrations in the microstructures of high-Cr steels. The nucleation of voids occurs when the critical value of the normal stress is exceeded at the particle-matrix interface.[62,63]

In addition, the microvoids appear on the boundaries of δ-ferrite grains because of the almost-continuous chains of particles. As a result, the network consists of semicontinuous chains of voids evolving along all types of HABs. The volume fraction of these voids is 0.7 pct. This value is close to that observed in tough P92-type steel.[24] However, in contrast to the present 12 pct Cr steel, the voids in side views of the Charpy specimens of P92-type steel were uniformly distributed along the boundaries of PAGs and packets; no semicontinuous chains of cavities appeared along the boundaries of PAGs.[24] As a result, the value of the impact toughness of P92 steel is 128 J even at – 65 °C.[22]

Aging leads to the formation of continuous chains of secondary phase particles along all boundaries of TMLS (Figure 4(c)). Almost-continuous chains of voids appear at these boundaries, and holes are observed at the site of δ-ferrite on the side views of the Charpy specimens (Figures 13(c) and (d)). The volume fraction of the voids increases to 1.9 pct owing to aging. Numerous

Table III. Sizes (mm) of Fracture Zones Determined on SEM Fractographs Along a Line Normal to the Notch at Mid-Thickness After Tempering (Numerator)/and Aging at 650 °C for 643 h (Denominator)

	Temperature (°C)								
Zone	– 20	0	5	20	50	100	150	200	250
Initiation Zone	0.10	0.18/0.06	0.16	0.18/0.19	0.18	0.19/0.32	—/0.14	0.25/0.16	—/0.22
Fibrous Zone	0	0.07/0	0.16	2.48/0.18	2.71	6.54/0.73	—/3.62	5.39/6.22	—/5.69
Unstable Crack Propagation Zone	7.89	7.65/7.83	7.64	4.58/7.32	2.85	0/5.54	—/1.39	0/0	—/0
Shear Lip Zone	0	0.09/0	0.09	0.78/0	2.66	1.79/1.35	—/2.56	2.73/2.13	—/2.28
Total	7.99	7.99/7.89	8.05	8.02/7.69	8.40	8.52/7.94	—/7.71	8.37/8.51	—/8.19
Percent Shear Fracture (pct)	0	2.63/0	7.69	28.51/2.10	75.02	100/44.76	—/92.39	100/100	—/100

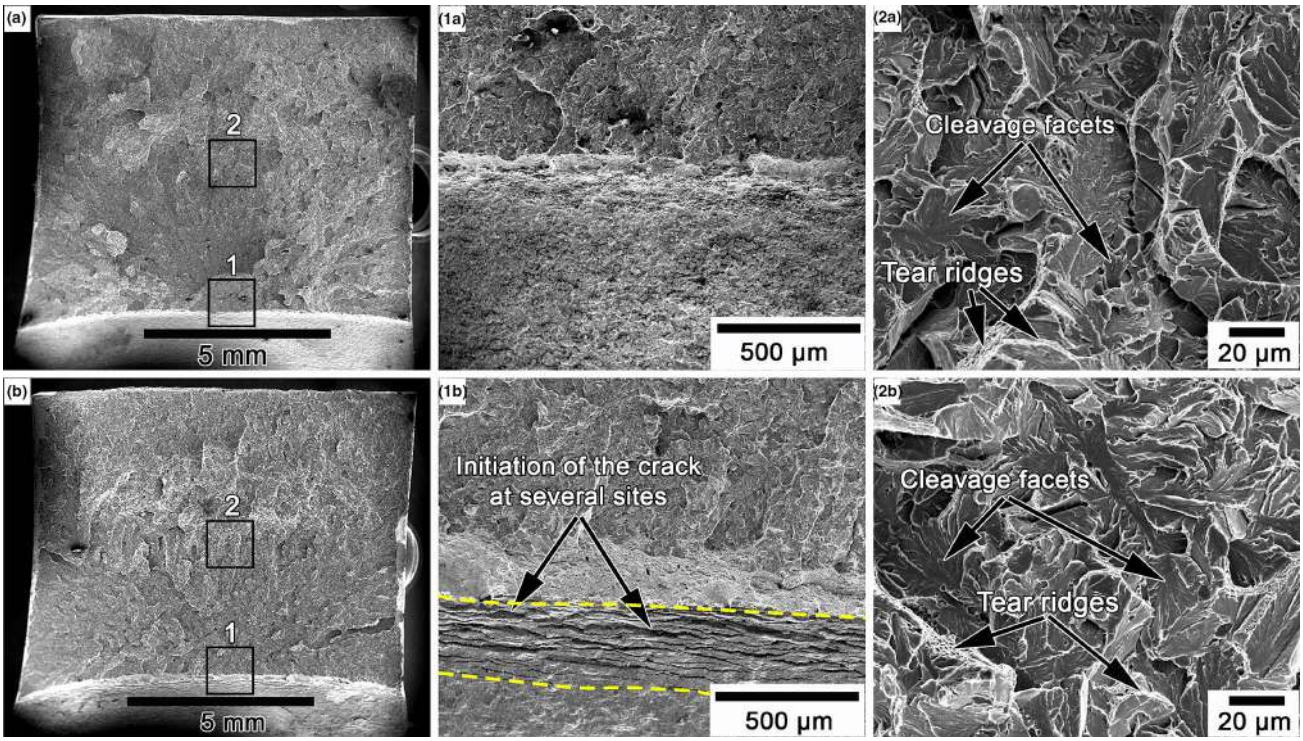

Fig. 12—Fracture surface of tempered and aged 12 pct Cr steel after impact tests at (*a*) − 20 °C and (*b*) 20 °C. (1a, 1b) SEM micrographs showing initiation of crack in area framed by number 1 in (a) and (b). (2a, 2b) High magnifications of brittle fracture surfaces in area framed by number 2 in (a) and (b).

nucleations of cavities on the $M_{23}C_6$ carbides and the Laves phase at boundaries leads to continuous chains of voids along the boundaries of PAGs and packets. It is worth noting that the cleavage fracture of χ-phase particles occurs within δ-ferrite grains (Figure 13(d)). However, subsequent propagation of the cracks is arrested because of a presence of a soft ductile ferrite matrix around the particles and the rapid blunting of the crack tip.

δ-Ferrite serves as an embrittlement agent owing to the dense particles on its boundaries.[66] Another embrittlement agent is the continuous chains of secondary phase particles on the boundaries of PAGs and packets.[63,67] Figure 14 schematically shows the particles and void distribution in the vicinity of the principal crack tip in the stable crack propagation zone for the tempered and aged steel.

It is known[68] that cracks serves as sites for stress concentration with the highest stress field ahead of the growing crack. As previously mentioned the internal stresses arise at the particles-matrix interface owing to the difference in the response of the particle and matrix to the applied stress. The stress concentration significantly increases the internal stress on the particle-matrix interface in the crack tip vicinity. The nucleation of voids takes place when the sum of the matrix yield stress and internal stress reaches the critical fracture stress at the particle-matrix interface (Figure 14(a)).[63] Next, this void grows. The ligament between the crack tip and the void is deformed and becomes thinner. The stress and strain fields at the crack tip that sweep over the near-tip material may promote the coalescence of the neighboring voids in the vicinity of the crack tip by cleavage of the ligaments. Aging decreases the interparticle distance owing to the additional precipitation of the Laves phase at the boundaries. Therefore, the thickness of the ligaments decreases, which promotes their cleavage at low temperatures and the formation of cracks with critical dimensions susceptible to unstable propagation.

The brittleness of the 12 pct Cr steel in a tempered condition is attributed to high $M_{23}C_6$ carbide density in packet, blocks, PAGs, and δ-ferrite boundaries, whereas the shift in the DBTT caused by aging is associated with the appearance of the Laves phase, which serves as an additional embrittlement agent. The role of these agents involves restricting the plastic deformation during the stable crack propagation stage. The boundary particles serve as effective barriers to the transmission of plastic deformation from one structural element (δ-ferrite, PAG, packet, or lath) to another. Hence the stress relaxation occurs by the nucleation of micro-cracks at the particle/matrix interface.

The transition from cleavage to the ductile mechanism of crack propagation is attributed to the competition between the propagation of a cleavage crack at a constant critical energy release rate and the nucleation of a dislocation loop on a highly stressed inclined slip plane going through the crack front.[69] If the barrier to the formation of a dislocation loop is high, the cleavage mechanism is in dominance. If the critical stress for the dislocation emission is low, then blunting of the crack tip owing to plastic deformation occurs extensively, and

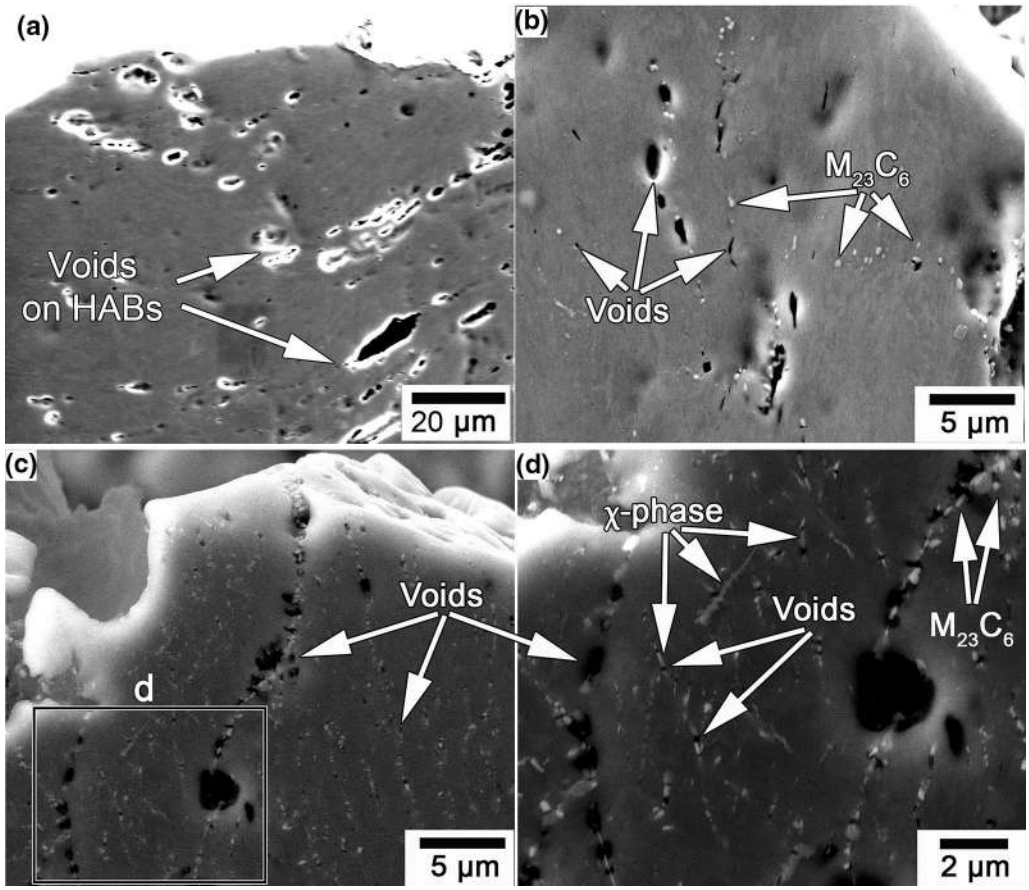

Fig. 13—Side-view SEM (secondary electron) images of Charpy specimens of (*a*, *b*) tempered and (*c*, *d*) aged steels fractured at temperatures of (a, b) 20 °C and (c, d) 100 °C.

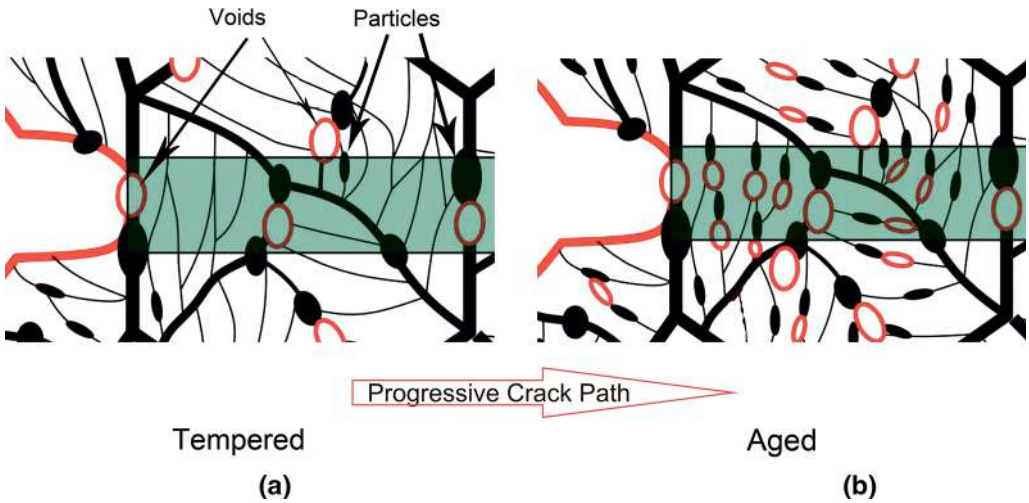

Fig. 14—Schematic illustration showing void distribution in vicinity of principal crack tip in stable crack propagation zone for (*a*) tempered and (*b*) aged 12 pct Cr steel.

the crack propagates in a ductile manner. An increased density of boundary particles promotes the formation of voids at these particles. At low temperatures, the blunting of the crack tips is hindered, and these voids facilitate crack growth. As a result, the length of the principal crack required for the onset of unstable crack propagation is attained at small dimensions of the fibrous zone. At high temperatures, dislocation glide occurs, promoting the blunting and coalescence of boundary voids that occur in a ductile manner. The effect of boundary particles on the Charpy V-notch absorbed energy is low. Thus, the boundary particles

promote the transition from stable crack propagation to unstable crack propagation that leads to a high DBTT and temperature of full embrittlement. At the same time, the appearance of continuous chains of secondary phase particles along the boundaries of PAGs and packets does not affect the temperature of full embrittlement, as the aging-induced precipitation significantly affects the propagation region and restricts the initial ductile fibrous zone.

V. CONCLUSIONS

Ductile-to-brittle transition in a novel 12 pct Cr steel modified by 4 pct Co and 0.8 pct Cu was studied after tempering and aging at 650 °C for 643 hours. The results can be summarized as follows:

1. The impact toughness of the 12 pct Cr steel modified by 4 pct Co and 0.8 pct Cu after normalizing at 1070 °C and tempering at 770 °C decreases from 250 J/cm^2 to 9 J/cm^2 with a decrease in the test temperature from 100 °C to − 20 °C. The ductile-brittle transition (DBT) temperature is 41 °C. The steel exhibits a relatively high impact toughness of 100 J/cm^2 at a temperature of 20 °C.
2. Aging at 650 °C for 643 hours leads to a significant increase in the DBT temperature to 122 °C. The steel exhibits a low value of impact toughness of 20 J/cm^2 at a temperature of 20 °C.
3. Particles of $M_{23}C_6$ carbides precipitated at the boundaries of the PAG, block, packet, and Laves phase at all types of boundaries serve as nucleation sites for micro-cracks/voids. Aging leads to an increase in the density of boundary particles. A shift of DBTT to a higher temperature is associated with a decrease in the average size of voids/dimples in the stable crack propagation zone owing to decreased interparticle spacing after aging.
4. The role of boundary particles in fractures consists of restricting plastic deformation and blunting the crack tip in the stable crack propagation zone that leads to an increased stress concentration in the vicinity of the crack tips. In addition, crack growth is promoted by the coalescence of voids nucleated on boundary particles. As a result, the critical stress at the crack tips for the onset of cleavage is reached after following a short propagation path.

ACKNOWLEDGMENTS

The study was supported by the Ministry of Education and Science of Russian Federation, under project of Government Task No. 11.2868.2017/PCh (number for publication 11.2868.2017/4.6). The authors are grateful to the staff of the Joint Research Center, «Technology and Materials», Belgorod State National Research University, for their technical assistance.

REFERENCES

1. K.-H. Mayer and F. Masuyama: in *Creep-Resistant Steels*, F. Abe, T.-U. Kern, and R. Viswanathan, eds., Woodhead Publishing and Maney Publishing, Cambridge, 2008, pp. 15–77.
2. R.O. Kaybyshev, V.N. Skorobogatykh, and I.A. Shchenkova: *Phys. Met. Metallogr.*, 2010, vol. 109, pp. 186–200.
3. R. Viswanathan and W. Bakker: *J. Mater. Eng. Perform.*, 2001, vol. 10, pp. 96–101.
4. F. Masuyama: *ISIJ Int.*, 2001, vol. 41 (6), pp. 612–25.
5. A. Pirscher, B. Scarlin, and R. Vanstone: in *Advances in Materials Technology for Fossil Power Plants—Proceedings from the 5th International Conference 2008*, R. Viswanathan, D. Gandy, and K. Coleman, eds., ASM International, Marco Island, 2008, pp. 338–52.
6. H. Kitahara, R. Ueji, N. Tsuji, and Y. Minamino: *Acta Mater.*, 2006, vol. 54, pp. 1279–88.
7. A. Kostka, K. Tak, R. Hellmig, Y. Estrin, and G. Eggeler: *Acta Mater.*, 2007, vol. 55, pp. 539–50.
8. V. Dudko, A. Belyakov, and R. Kaibyshev: *ISIJ Int.*, 2016, pp. 3–6.
9. H. Ghassemi-Armaki, R.P. Chen, K. Maruyama, and M. Igarashi: *J. Nucl. Mater.*, 2013, vol. 433, pp. 23–29.
10. R. Mishnev, N. Dudova, A. Fedoseeva, and R. Kaibyshev: *Mater. Sci. Eng. A*, 2016, vol. 678, pp. 178–89.
11. R. Mishnev, N. Dudova, and R. Kaibyshev: *Mater. Sci. Eng. A*, 2018, vol. 713, pp. 161–73.
12. M. Mitsuhara, S. Yamasaki, M. Miake, H. Nakashima, M. Nishida, J. Kusumoto, and A. Kanaya: *Philos. Mag. Lett.*, 2016, vol. 96, pp. 76–83.
13. K. Maruyama, K. Sawada, and J. Koike: *ISIJ Int.*, 2001, vol. 41, pp. 641–53.
14. V. Dudko, A. Belyakov, and R. Kaibyshev: *Mater. Sci. Forum*, 2012, vols. 706–709, pp. 841–6.
15. A. Fedoseeva, N. Dudova, R. Kaibyshev, and A. Belyakov: *Metals (Basel)*, 2017, vol. 7, p. 573.
16. Q. Lu, W. Xu, and S. Van Der Zwaag: *Acta Mater.*, 2014, vol. 77, pp. 310–23.
17. S. Sathyanarayanan, J. Basu, A. Moitra, G. Sasikala, and V. Singh: *Metall. Mater. Trans. A*, 2013, vol. 44A, pp. 2141–55.
18. X. Hu, L. Huang, W. Yan, W. Wang, W. Sha, Y. Shan, and K. Yang: *Mater. Sci. Eng. A*, 2013, vol. 586, pp. 253–58.
19. W. Zhong, W. Wang, X. Yang, W. Li, W. Yan, W. Sha, and W. Wang: *Mater. Sci. Eng. A*, 2015, vol. 639, pp. 252–58.
20. W. Wang, W. Yan, W. Sha, Y. Shan, and K. Yang: *Metall. Mater. Trans. A*, 2012, vol. 43A, pp. 4113–22.
21. G. Sasikala and S.K. Ray: *Mater. Sci. Eng. A*, 2008, vol. 479, pp. 105–11.
22. V. Dudko, A. Fedoseeva, and R. Kaibyshev: *Mater. Sci. Eng. A*, 2017, vol. 682, pp. 73–84.
23. A. Fedoseeva, N. Dudova, and R. Kaibyshev: *Metall. Mater. Trans. A*, 2017, vol. 48A, pp. 982–98.
24. R. Mishnev, N. Dudova, V. Dudko, and R. Kaibyshev: *Mater. Sci. Eng. A*, 2018, vol. 730, pp. 1–9.
25. A. Chatterjee, D. Chakrabarti, A. Moitra, R. Mitra, and A.K. Bhaduri: *Mater. Sci. Eng. A*, 2015, vol. 630, pp. 58–70.
26. K.C. Sahoo, J. Vanaja, P. Parameswaran, V.D. Vijayanand, and K. Laha: *Mater. Sci. Eng. A*, 2017, vol. 686, pp. 54–64.
27. T.S. Byun, D.T. Hoelzer, J.H. Kim, and S.A. Maloy: *J. Nucl. Mater.*, 2017, vol. 484, pp. 157–67.
28. R. Blum and R.W. Vanstone: in *Materials for Advanced Power Engineering 2006. Proceedings Part I*, J. Lecomte-Beckers, M. Carton, F. Schubert, and P.J. Ennis, eds., Forschungszentrum Jülich GmbH, 2006, pp. 41–60.
29. K. Anderko, L. Sch, and A.K. Ewaiom: *J. Nucl. Mater.*, 1991, vols. 179–181, pp. 492–5.
30. Y. Hosoi, N. Wade, S. Kunimitsu, and T. Urita: *J. Nucl. Mater.*, 1986, vols. 141–143, pp. 461–67.
31. J. Blach, L. Falat, and P. Ševc: *Eng. Fail. Anal.*, 2009, vol. 16, pp. 1397–403.
32. S. Komazaki, T.S. Shigeo Kishi, H. Chiba, and K. Suzuki: *Mater. Sci. Res. Int.*, 2003, vol. 9, pp. 919–26.
33. P. Yan and Z. Liu: *Mater. Sci. Eng. A*, 2016, vol. 650, pp. 290–94.
34. ASTM E 23-12c: *Standards*, 2013, vol. i, pp. 1–25.
35. V. Dudko, A. Belyakov, D. Molodov, and R. Kaibyshev: *Metall. Mater. Trans. A*, 2013, vol. 44A, pp. 162–72.

36. A. Fedoseeva, N. Dudova, and R. Kaibyshev: *J. Mater. Sci.*, 2017, vol. 52, pp. 2974–88.
37. Y.I. Borisova, V.A. Dudko, V.N. Skorobogatykh, I.A. Shchenkova, and R.O. Kaibyshev: *Phys. Met. Metallogr.* https://doi.org/10.1134/S0031918X1708004X.
38. A. Fedoseeva, I. Nikitin, N. Dudova, and R. Kaibyshev: *Mater. Lett.*, 2019, vol. 236, pp. 81–84.
39. S.S. Wang, L. Chang, L. Wang, T. Wang, Y.D. Wu, J.J. Si, J. Zhu, M.X. Zhang, and X.D. Hui: *Mater. Sci. Eng. A*, 2015, vol. 622, pp. 204–11.
40. T. Vershinina and M. Leont-Smirnova: *Mater. Charact.*, 2017, vol. 125, pp. 23–28.
41. S. Wang, L. Chang, D. Lin, X. Chen, and X. Hui: *Metall. Mater. Trans. A*, 2014, vol. 45A, pp. 4371–85.
42. S. Li, Z. Eliniyaz, X. Dong, Y. Shen, L. Zhang, and A. Shan: *Mater. Sci. Eng. A*, 2013, vol. 580, pp. 51–57.
43. J. Hald: in *Materials for Ultra-Supercritical and Advanced Ultra-Supercritical Power Plants*, A. Di Gianfrancesco, ed., Elsevier Ltd, 2016, pp. 77–97.
44. C. Cui, X. Gao, G. Su, C. Gao, Z. Liu, and R.D.K. Misra: *Mater. Sci. Technol.* (*United Kingdom*), https://doi.org/10.1080/02670836.2018.1510072.
45. F.-G. Wei, T. Hara, and K. Tsuzaki: *Philos. Mag.*, 2004, vol. 84, pp. 1735–51.
46. M. Taneike, K. Sawada, and F. Abe: *Metall. Mater. Trans. A*, 2004, vol. 35A, pp. 1255–62.
47. N. Dudova, A. Plotnikova, D. Molodov, A. Belyakov, and R. Kaibyshev: *Mater. Sci. Eng. A*, 2012, vol. 534, pp. 632–39.
48. M. Shibuya, Y. Toda, K. Sawada, H. Kushima, and K. Kimura: *Mater. Sci. Eng. A*, 2011, vol. 528, pp. 5387–93.
49. A. Fedoseeva, N. Dudova, and R. Kaibyshev: *Mater. Sci. Eng. A*, 2016, vol. 654, pp. 1–12.
50. Y. Toda, K. Seki, K. Kimura, and F. Abe: *ISIJ Int.*, 2003, vol. 43, pp. 112–18.
51. M. Rashidi, L. Johansson, H.O. Andrén, and F. Liu: *Mater. Sci. Eng. A*, 2017, vol. 694, pp. 57–65.
52. M. Hättestrand and H.O. Andrén: *Mater. Sci. Eng. A*, 2001, vol. 318, pp. 94–101.
53. M.G. Park, C.H. Lee, J. Moon, J.Y. Park, T.H. Lee, N. Kang, and H. Chan Kim: *J. Nucl. Mater.*, 2017, vol. 485, pp. 15–22.
54. W. Wang, S. Liu, G. Xu, B. Zhang, and Q. Huang: *Nucl. Eng. Technol.*, 2016, vol. 48, pp. 518–24.
55. *ASM Handbook, Volume 8, Mechanical Testing and Evaluation*, ASM International, 2000.
56. Chaouadi R. and Fabry A.: in *From Charpy to Present Impact Testing*, D. Franqois and A. Pineau, eds., 1st ed., Elsevier Science Ltd. and ESIS, Oxford, 2002, pp. 103–17.
57. A. Dolzhenko, Z. Yanushkevich, S.A. Nikulin, A. Belyakov, and R. Kaibyshev: *Mater. Sci. Eng. A*, 2018, vol. 723, pp. 259–68.
58. M.V. Odnobokova, A.Y. Kipelova, A.N. Belyakov, and R.O. Kaibyshev: *Phys. Met. Metallogr.*, 2016, vol. 117, pp. 390–98.
59. F. Zia-Ebrahimi and G. Krauss: *Metall. Trans. A*, 1983, vol. 14A, pp. 1109–19.
60. *ASM Handbook, Volume 12, Fractography*, ASM International, 1987.
61. A. Das: *Philos. Mag.*, 2017, vol. 97, pp. 3084–141.
62. G. Le Roy, J.D. Embury, G. Edwards, and M.F. Ashby: *Acta Metall.*, 1981, vol. 29, pp. 1509–22.
63. L.M. Brown and S.H. Goods: *Acta Metall.*, 1979, vol. 27, pp. 1–15.
64. A. Das and C.B. Basak: *Philos. Mag.*, 2018, vol. 98, pp. 3007–33.
65. A. Das, SK. Das, and S Tarafder: *Metall. Mater. Trans. A*, 2009, vol. 40A, pp. 3138–46.
66. K.J. Harrelson, S.H. Rou, and R.C. Wilcox: *J. Nucl. Mater.*, 1986, vols. 141–143, pp. 508–12.
67. D. Broek: *Eng. Fract. Mech.*, 1973, vol. 5, pp. 55–66.
68. A. Needleman and V. Tvergaard: *J. Mech. Phys. Solids*, 1987, vol. 35, pp. 151–83.
69. A.S. Argon: *Acta Metall.*, 1987, vol. 35, pp. 185–96.